Junseok Hong[1*], Hyosub Kil[2], Woo Kyoung Lee[1,3], Young-Sil Kwak[1,3], Byung-Kyu Choi[1], and Larry J. Paxton[2]

[1]Korea Astronomy and Space Science Institute, Daejeon, South Korea

[2]Johns Hopkins University Applied Physics Laboratory, Maryland, United States

[3]University of Science and Technology, Daejeon, South Korea

Corresponding author: Junseok Hong (junseok@kasi.re.kr)

Key Points:

- Moderate and intense total electron content perturbations are detected to the west and south of Korea about 8 hours after eruption
- Perturbations to the west are consistent with surface air pressure perturbations and propagate away from the epicenter with 302 m/s speed
- Intense perturbations to the south are associated with the poleward extension of equatorial plasma bubbles triggered by the eruption

Abstract

This study reports two different properties of ionospheric perturbations detected to the west and south of the Korean Peninsula after the Hunga-Tonga volcanic eruption on 15 January 2022. Transient wave-like total electron content (TEC) modulations and intense irregular TEC perturbations are detected in the west and south of the Korean Peninsula, respectively, about eight hours after the eruption. The TEC modulations in the west propagate away from the epicenter with a speed of 302 m/s. Their occurrence time, propagation direction and velocity, and alignment with the surface air pressure perturbations indicate the generation of the TEC modulations by Lamb waves generated by the eruption. The strong TEC perturbations and L band scintillations in the south are interpreted in terms of the poleward extension of equatorial plasma bubbles (EPBs). We demonstrate the association of the EPBs with volcanic eruption using the EPB occurrence climatology derived from Swarm satellite data.

Plain Language Summary

A massive eruption of Hunga Tonga–Hunga Ha'apai volcano on 15 January 2022 left its footprint as various perturbations in the atmosphere and ionosphere. We identified two types of ionospheric perturbations over Korea. One is a transient wave-like perturbation detected to the west, and the other is a more substantial one detected to the south, including L band scintillation. Both disturbances occurred about 8 hours after the eruption. The development of different ionospheric perturbations in two regions is related to their generation mechanisms. The former is associated with the modulation of the ionospheric height by atmospheric waves, but the latter is attributed to the plasma instabilities triggered by atmospheric waves. The consistent behavior of atmospheric and ionospheric

perturbations and the development of severe storms in low latitude ionosphere support these interpretations.

1 Introduction

An explosive submarine volcanic eruption occurred at 04:15 universal time (UT) on 15 January 2022 at Hunga Tonga-Hunga Ha'apai (hereafter Hunga-Tonga) (Longitude 175.38°W, Latitude: 20.54°S). The volcanic explosivity index (VEI) of this event is estimated to be 5 or 6. This magnitude of eruption is comparable to the St. Helens volcano (VEI 5) in the United States on 18 May 1980 and the Pinatubo volcano (VEI 6) in the Philippines on 15 June 1991. The Hunga-Tonga event primarily draws attention from the aeronomy community because of its global impact on the atmosphere. The observations of its footprint worldwide provide an unprecedented opportunity to assess the generation and propagation of various atmospheric waves and their effect on the ionosphere (Aa et al., 2022; Amores et al., 2022; Harding et al., 2022; Themens et al., 2022; Wright et al., 2022). The total electron content (TEC) measurements from the dense Global Navigation Satellite System (GNSS) network on the ground provide a means to trace near- and far-field atmospheric waves. This capability is one of the distinguishing points of the Hunga-Tonga event from earlier St. Helens and Pinatubo events.

Volcanic eruptions produce atmospheric waves over a wide range of frequencies (Astafyeva, 2019). Low-frequency acoustic waves generated primarily by the rapid release of overpressure or continuous mass ejection (Johnson, 2007) can propagate over large distances because of their low attenuation rate (Matoza et al., 2011). TEC perturbations caused by acoustic waves have been detected far from the epicenter, depending on the event's magnitude. For example, the Asama volcano eruption in Central Japan on 1 September 2004, recorded as VEI 2, produced up to 0.16 total electron content units (TECU, 1 TECU=10^{16} m^{-2}) perturbations within a few hundred kilometers from the epicenter (Heki, 2006). The VEI 3 Soufrière Hill volcano eruption in the Caribbean on 13 July 2003 produced about 0.15 TECU perturbations within 500 km from the epicenter (Dautermann et al., 2009). More substantial TEC perturbations from 0.4 to 0.45 TECU were reported within 800 km from the epicenter for the 4 VEI events; Kelud volcano in Indonesia on 13 February 2014 (Nakashima et al., 2016) and Calbuco volcano in Chile on 22–23 April 2015 (Shults et al., 2016). VEI 5 level eruptions perturb the global ionosphere. The St. Helens eruption (VEI 5) on 18 May 1980 created TEC perturbations more than 8000 km distance from the epicenter (Liu et al., 1982), and the Pinatubo eruption (VEI 6) on 15 June 1991 produced TEC perturbations of a few TECU for horizontal distances over 1000 km (Cheng & Huang, 1992; Igarashi et al., 1994).

We identified two types of TEC perturbations in the vicinity of the Korean Peninsula after the Hunga-Tonga volcanic eruption on 15 January 2022. The first one is wave-like TEC perturbations with moderate levels (~0.2 TECU) around 12 UT to the west of Korea. These perturbations lasted only 10 min and did not produce L band scintillations. The second one is severe TEC perturbations (~1

TECU) at a similar UT to the south of Korea. However, latter perturbations persisted for more than three hours and produced strong L band scintillations. This study investigates the generation mechanisms of different characteristics of TEC perturbations in the two regions by analyzing GNSS TEC and scintillation data, measurements of the surface air pressure over South Korea, and Swarm satellite data.

2 Data and Method

This study examines ionospheric perturbations around the Korean Peninsula using TEC and scintillation index S_4. First, we derive slant TEC using Global Positioning System data from 36 GNSS stations in Korea. The detailed description of TEC estimation is referred to Choi et al. (2017, 2019). Second, detrended TEC (dTEC) is derived from slant TEC after removing the background TEC using the Savitzky–Golay filter (Savitzky and Golay, 1964). Because 30 min window is appropriate for extracting large-scale TEC perturbations (Zhang et al., 2017; Zhang et al., 2019), we apply a 30 min running average window to derive dTEC. The time resolution of the dTEC data is 1 s. Third, the scintillation index (S_4) is derived from the 50 Hz L band signal amplitude obtained from 2 GNSS scintillation stations. We set the elevation cutoff angle to 30° to reduce multipath errors in deriving TEC and S_4 but lower it to 15° in making Figure 1 to extend the observation area. The trajectory of GNSS satellites is projected to a 300 km ionospheric pierce point (IPP) altitude.

The automatic weather station (AWS) network in South Korea provides surface air pressure data, and we estimate the propagation speed of shock waves from those data. The Korea Meteorological Administration operates 503 AWS, and this study uses the data from 10 AWS sites. We select sites as a function of the distance from the epicenter. The data cadence of the surface air pressure is 60 s. We infer the atmosphere-ionosphere interaction by comparing the propagation speed of atmospheric waves estimated from dTEC and surface air pressure.

Swarm is a constellation of three satellites (Friis-Christensen et al., 2008) launched on 22 November 2013. The altitude of Swarm-A and Swarm-C is 470 km with an inclination of 87.5°, while Swarm-B's is 530km with an 88° inclination angle. The time resolution of the data is 0.5 s. This study uses the Swarm data in January in four years (2014, 2018, 2019, and 2022) to assess the probability of electron density irregularities in low latitudes.

3 Results

The distance of the great circle between the epicenter of the Hunga-Tonga volcanic eruption and the middle of South Korea is approximately 8700 km. Perturbations in the atmosphere and ionosphere in the vicinity of the Korean Peninsula started to emerge around 12 UT, about eight hours after the volcanic eruption. Roughly, the propagation speed of atmospheric waves near Korea is about 300 m/s. This velocity is consistent with the velocities of Lamb waves detected after the Mount St. Helens volcanic eruption on 18 May 1980 (Liu et al., 1982) and the Hunga-Tonga eruption (Amores et al., 2022; Wright et al., 2022). The

model simulations of the Hunga-Tonga event also showed the propagation of Lamb waves with a velocity of about 300 m/s (Themens et al., 2022).

Figure 1 provides an overview of the ionospheric perturbations around 12 UT on 15 January 2022. The dTEC data (color scale) along the trajectories of PRN 3, 7, 17, and 30 are shown in Figure 1a as a function of the distance from the epicenter and UT. The dTEC perturbations greater than 1 TECU are indicated by red dots. The surface air pressure measurements at three stations in South Korea are shown with thick blue lines to compare the ionospheric and atmospheric perturbations. The distances from the epicenter are calculated at the Earth's surface for the surface air pressure and 300 km IPP altitude for the dTEC data. From the dTEC perturbations between 12 and 13 UT (indicated with a black arrow), we can identify a few cycles of dTEC modulations and the alignment of the modulations in the direction of increasing distance and UT. These perturbations are detected to the west of the Korean Peninsula. About two hPa perturbations are clearly visible from the surface air pressure data, and these perturbations are well aligned with the TEC modulations. The TEC perturbations indicated by red arrows reveal different characteristics. These perturbations, detected in the south of Korea, are more intense compared with the perturbations noted by the black arrow and do not show wave characteristics.

The trajectories of the four satellites in Figure 1a are shown in Figure 1b with the dTEC data along the trajectories. The dTEC data in the map are for 11–14 UT. The vertical blue line is the Swarm-C pass around 15 UT with the location (thick line) of strong irregularities. The green dots are the satellite trajectories for the S_4 index in Figure 1c. For PRN 7 and 30, their trajectories above 35°N are not plotted to avoid overlapping with the PRN 17 trajectories. The dTEC perturbations at 120°–125°E longitude in the PRN 17 trajectories correspond to the dTEC modulations at 12–13 UT in Figure 1a. Along the PRN 7 and 30 trajectories, the boundary of the wave-like modulations (indicated by the black arrow in Figure 1a) and intense random perturbations (indicated by red arrows in Figure 1a) occurs at approximately 30°N. Strong TEC perturbations are recorded along the PRN 3, 7, and 30 trajectories equatorward of 30°N. Although the elevation angles of these satellites equatorward of 30°N are mostly less than 30°, the strong TEC perturbations detected in that region are interpreted as actual perturbations (not due to the low satellite elevation angle) because this level of TEC perturbations is seen only on 15 January 2022.

The S_4 indices from PRN 17 (red) and 30 (green) along the green dot trajectories in Figure 1b are compared in Figure 1c. The S_4 data obtained from low elevations (15°–30°) are distinguished by dashed lines. The S_4 indices from PRN 30 are a few times greater than those from PRN 17 at the locations where severe TEC perturbations are recorded. The wave-like TEC modulations in the PRN 17 trajectories do not produce L band scintillations regardless of the satellite elevation. Considering the small S_4 indices at low elevations of PRN 17, the large S_4 indices at low elevations of PRN 30 are not attributed to geometric factors such as multipath. Thus, the scintillation measurements also indicate

different characteristics of ionospheric perturbations to the west and south of the Korean Peninsula. The Swarm-C observation of the electron density (black) in Figure 1d provides a clue as to the cause of the strong scintillation south of 30°N. Severe irregularities that look like equatorial plasma bubbles (EPBs) appear in the Swarm-C data at low latitudes. The irregularity index "S" (red) is the standard deviation of the logarithm of the density derived using 10 s (20 points) data (Kil et al., 2019; Kil et al., 2020). The blue horizontal line at the 17°S–30°N interval indicates the irregularity location. The northern boundaries of the irregularities in the Swarm-C data and strong scintillations and TEC perturbations in Figure 1b are consistent. We note the three-hour difference between the Swarm-C (15 UT) and TEC (12 UT) observations. Although we do not have direct evidence of the development of similar levels of irregularities in the equatorial region around 12 UT, we can infer their existence before 12 UT from the detection of strong scintillations to the south of 30°N. The persistence of strong ionospheric perturbations for more than three hours in the south is distinguished from the observation of transient TEC modulations for less than 10 minutes west of Korea.

We further explore the characteristics of the TEC perturbations west of Korea by comparing the surface air pressure data. The line plots of dTEC data from PRN 17 (red) and PRN 3 (magenta) and the surface air pressure data (blue) are shown in Figure 2a as a function of the distance and UT. PRN 7 and 30 data are not shown to avoid overlapping with the surface air pressure data. The slant black line approximately connects the peaks in the dTEC and surface air pressure data. The distances are from the epicenter to the locations of the peak dTEC and surface air pressure values. As we can identify from the PRN 3 data (magenta), the peak locations are not meaningful for the PRN 3 data because the TEC perturbations fluctuate randomly. Here we present the PRN 3 data to emphasize the difference between the TEC perturbations west (PRN 17) and south (PRN 3) of Korea. The dTEC perturbations in PRN17 data are well aligned with the surface air pressure perturbations, whereas wave characteristics are absent in the PRN 3 data.

We derive the propagation velocity of atmospheric waves using the distance and occurrence UT of the peak values in the surface air pressure and PRN 7, 17, and 30 dTEC data. The velocities obtained from each station's surface air pressure data are shown with blue dots in Figure 2b. The velocities derived from PRN 7 (purple), 17 (red), and 30 (green) are shown with filled triangles. The horizontal blue and red lines are the mean velocities derived from the surface air pressure and dTEC data, respectively. Although the velocities are derived from independent datasets, they show good agreement. The mean velocity of all data is near 302 m/s with a variation of less than 10 m/s. The black line in Figure 2a corresponds to this velocity. This velocity is comparable to the Lamb wave velocity of 305 m/s at about 7000–8000 km distance from the Mount St. Helens volcanic eruption on 18 May 1980 (Liu et al., 1982) and is also within the range of velocity (300–350 m/s) derived from the observations at other locations for the Hunga Tonga eruption (Zhang et al., 2022). The surface air pressure

and some of the PRN 17 dTEC data are plotted together in Figure 2c using the times of their peak values as an epoch. The duration of the surface air pressure is about 20 minutes, whereas the duration of dTEC impulse is several minutes. Right now, we do not have a good understanding of the cause of this duration difference. Because atmospheric perturbations at higher altitudes can be different from those at the surface, the surface air pressure data are not sufficient to specify the detailed plasma-neutral interaction.

4 Discussion

The generation of the wave-like TEC modulations seen west of Korea by the impact of the volcanic eruption is manifested in many observations. First, the TEC perturbations are detected at the predicted arrival times of Lamb waves. Second, the propagation speed and direction of the TEC perturbations are consistent with those derived from other observations for this event (Amores et al., 2022; Themens et al., 2022; Zhang et al., 2022). Third, the consistent behavior of the TEC and surface air pressure perturbations demonstrates the simultaneous generation of atmospheric perturbations from the Earth's surface to above 300 km altitude, and the volcanic eruption is the most plausible source. The coincident occurrence of atmospheric and ionospheric perturbations indicates the instantaneous ionospheric response to atmospheric perturbations.

The generation of strong TEC perturbations south of Korea is also interpreted in terms of the volcanic eruption, but its demonstration is not straightforward because wave characteristics are absent in the TEC perturbations. The Swarm-C observation in Figure 1d reveals the development of severe density irregularities in low latitudes, including the formation of a large density hole near the magnetic equator. We understand this density hole is produced by the uplift of the F-region peak height above the Swarm-C orbit (470 km altitude). Some of the irregularities look like EPBs. But some of them may be irregularities in the bottom side of the F region. Traveling ionospheric disturbances would also produce irregularities. Here we use the terminology "EPBs" as a collective representation of significant amplitude irregularities in the equatorial region regardless of their origin. Our primary interest is to identify whether volcanic eruption triggers the EPBs. The EPBs in the Asian sector are considered to be associated with the volcanic eruption because EPBs rarely occur in January in the Asian sector (Aa et al., 2020; Burke et al., 2004; Gentile et al., 2011; Huang et al., 2001; Kil & Heelis, 1998; Kil et al., 2009; McClure et al., 1998; Maruyama & Matuura, 1984; Stolle et al., 2006; Su et al., 2006; Tsunoda, 1985). However, we cannot rule out the generation of EPBs by other sources. A more rigorous investigation is necessary to demonstrate its "rareness".

The likelihood of EPBs at 20–00 LT in January in the Asian sector (100°–140°E) is investigated using the latitudinal distribution of EPBs derived from Swarm-C data. We choose this LT and longitude to validate our interpretation of the TEC perturbations detected before midnight around 120°E longitude as the poleward edge of EPBs. Figure 3 presents the latitudinal distribution of the S parameter as a function of day in January in four years: (a) 2014, (b) 2018,

(c) 2019, and (d) 2022. These are the years during which at least one Swarm satellite had orbits before midnight for more than 20 days. Because the results obtained from three Swarm satellites are not much different, the results from only one satellite are presented each year. Red lines show the daily mean Kp indices. The figure shows the pronounced S parameter during the four-year periods on only two days: 25 January 2014 and 15 January 2022 (event day). In 2014, Swarm-C data are absent on three days (13, 20, and 22). Because we have identified the absence of EPBs on 13 and 22 from Swarm-B data, EPB data are missing only for one day (20) in 2014. In 2022, we have no information on EPBs in the equatorial region on three days (1, 2, and 3). Excluding these four days and the event day, EPBs appear on one day (25 January 2014) out of 119 days. It corresponds to 0.84 % occurrence rate, and this small number can be used as a demonstration of the rarity of EPBs in January. In other words, the development of EPBs on 15 January 2022 by sources other than the volcanic eruption is unlikely. The development of the EPBs on that day can be understood in association with the geomagnetic storm on the previous day. However, the EPBs are detected during the recovery phase, about 12 hours after the end of the storm's main phase. Therefore, the development of EPBs is not likely to be associated with storm-induced electric fields (Harding et al., 2022). As Figures 3a–3d reveal, the occurrence and strength of irregularities do not show any correlation with the Kp index. Because geomagnetic activities either promote or suppress the development of EPBs, the occurrence rate of EPBs does not show a notable dependence on them.

Figure 3e shows the electron density data from Swarm-C on a disturbed day (25 January) in 2014. There were two Swarm-C passes within 100°–140°E longitude on that day, but EPBs were detected only in one pass shown in Figure 3e. The Swarm-C data were noisy in both orbits outside the equatorial region. The large S values at 30°–40°N are attributed to the data noise. EPBs appear near the magnetic equator. We have not yet found a reasonable explanation for the occurrence of EPBs on 25 January 2014. There was no geomagnetic activity on that day. Instead, an M6.1 earthquake occurred at 05:14 UT on that day near Indonesia (Latitude: 7.98°N, Longitude: 109.25°E), but this study cannot identify the connection of the EPBs with this earthquake. We did not find any other notable surface or meteorological event on that day.

The Asian sector was moving into the night at the time of the arrival of the observed atmospheric waves. Thus, atmospheric perturbations driven by the volcanic eruption were timely for developing EPBs. The formation of sizable equatorial density holes in the equatorial region in Swarm-C observations in Figure 1d indicates the uplift of the F region by eastward electric fields. The diagram in Figure 4 schematically illustrates the generation of eastward electric fields by atmospheric waves. Westward winds ($\boldsymbol{U}$) caused by the volcanic eruption generate the Hall current ($\boldsymbol{J}_H$) in the E region, and the day-night difference in the current induces the polarization electric fields ($\boldsymbol{E}$). Mapping of these electric fields to the F region drives the upward $\boldsymbol{E}\times\boldsymbol{B}$ plasma drift on the sunlit side. Its role is similar to the pre-reversal enhancement in the vertical plasma

motion on typical quiet days.

Harding et al. (2022) reported equatorial electrojet perturbations in the American sector after the Hunga-Tonga eruption. They interpreted this phenomenon in terms of electric fields driven by zonal winds in the dynamo region (90–150 km altitude). This interpretation parallels our interpretation of EPBs in the Asian sector by dynamo electric fields. We emphasized the E region dynamo driven by Hall current, but the dynamo driven by Pedersen current at higher altitudes would also affect the ionospheric dynamics. A complete understanding of the complex dynamo process requires numerical calculations with realistic observation data. In addition to the generation of dynamo-electric fields, atmospheric waves can provide initial seed perturbations for the development of EPBs (Aa et al., 2022). Considering the generation of a large density hole at the magnetic equator along with EPBs in the Asian sector, the dynamo process was effective in the region regardless of the role of the seeding mechanism.

5 Conclusions

We identify two different properties of TEC perturbations in the west and south of Korea about eight hours after the Hunga-Tonga volcanic eruption on 15 January 2022. Transient wave-like TEC modulations are observed in the west of Korea, and intense TEC perturbations accompanied by strong scintillations are detected in the south of Korea. The TEC modulations at the west propagate away from the epicenter with a velocity of 302 m/s. Their generation time, propagation speed and direction, and good agreement with the perturbations in the surface air pressure indicate their generation by the Lamb waves produced by the eruption. These TEC perturbations did not produce L band scintillations. The intense TEC perturbations at the south show random fluctuations, so wave characteristics are not identified. The Swarm satellite observations reveal the development of severe EPBs in the equatorial region in the Asian sector. Thus, the TEC perturbations south of Korea are understood as a detection of the poleward edge of the EPBs. The occurrence climatology of irregularities derived from Swarm satellite data demonstrates that the generation of the EPBs on that day by sources other than the volcanic eruption is unlikely. We suggest that eastward polarization electric fields generated by westward propagating atmospheric waves cause the uplift of the ionosphere and trigger the development of intense EPBs. Numerical simulations will provide further insight into our understanding of the propagation of waves from the epicenter and its impact on the atmosphere and ionosphere.

Acknowledgments

This study was supported by a basic research fund from the Korea Astronomy and Space Science Institute (KASI) (2022185010). H. Kil and L. J. Paxton were supported by grants from NSF-AGS2029840 and United States Air Force MURI FA9559-16-1-0364 and AOARD FA2386-21-1-4034.

The GNSS data provided by Korea Astronomy and Space Science Institute are available on the website (https://gnss.kasi.re.kr). Swarm satellite data

are available on the website of the European Space Agency (ESA; http://swarm-diss.eo.esa.int/). The meteorological data of automatic weather station (AWS) network data by the Korea Meteorological Administration (KMA) are available on the website (https://www.weather.go.kr/weather/observation/aws_graph_popup.jsp). Kp index data were obtained from OMNIWeb (https://omniweb.gsfc.nasa.gov/form/dx1.html).

References

Aa, E., Zou, S., & Liu, S. (2020). Statistical Analysis of Equatorial Plasma Irregularities Retrieved From Swarm 2013–2019 Observations. *Journal of Geophysical Research: Space Physics, 125*(4), https://doi.org/10.1029/2019ja027022

Amores, A., Monserrat, S., Marcos, M., Argüeso, D., Villalonga, J., Jordà, G. et al. (2022). Numerical Simulation of Atmospheric Lamb Waves Generated by the 2022 Hunga-Tonga Volcanic Eruption. *Geophysical Research Letters*, *49*(6), https://doi.org/10.1029/2022gl098240

Astafyeva, E. (2019). Ionospheric Detection of Natural Hazards. *Reviews of Geophysics, 57*(4), 1265–1288. https://doi.org/10.1029/2019rg000668

Burke, W. J. (2004). Longitudinal variability of equatorial plasma bubbles observed by DMSP and ROCSAT-1. *Journal of Geophysical Research, 109*(A12), https://doi.org/10.1029/2004ja010583

Cheng, K., & Huang, Y.-N. (1992). Ionospheric disturbances observed during the period of Mount Pinatubo eruptions in June 1991. *Journal of Geophysical Research, 97*(A11), 16995. https://doi.org/10.1029/92ja01462

Choi, B.-K., & Kil, H. (2017). Large ionospheric TEC depletion induced by the 2016 North Korea rocket. *Advances in Space Research, 59*(2), 532–541. https://doi.org/10.1016/j.asr.2016.09.012

Choi, B.-K., & Hong, J. (2019). Observation of the fast-traveling ionospheric disturbances induced by the 2017 North Korean missile. *Advances in Space Research, 63*(8), 2598–2608. https://doi.org/10.1016/j.asr.2018.12.033

Dautermann, T., Calais, E., & Mattioli, G. S. (2009). Global Positioning System detection and energy estimation of the ionospheric wave caused by the 13 July 2003 explosion of the Soufrière Hills Volcano, Montserrat. *Journal of Geophysical Research, 114*(B2), https://doi.org/10.1029/2008jb005722

Friis-Christensen, E., Lühr, H., Knudsen, D., & Haagmans, R. (2008). Swarm – An Earth Observation Mission investigating Geospace. *Advances in Space Research, 41*(1), 210–216. https://doi.org/10.1016/j.asr.2006.10.008

Gentile, L. C., Burke, W. J., Roddy, P. A., Retterer, J. M., & Tsunoda, R. T. (2011). Climatology of plasma density depletions observed by DMSP in the dawn sector. *Journal of Geophysical Research: Space Physics, 116*(A3), https://doi.org/10.1029/2010ja016176

Harding, B. J., Wu, Y.-J. J., Alken, P., Yamazaki, Y., Triplett, C., Immel, T. J. et al. (2022). Impacts of the January 2022 Tonga volcanic eruption on the ionospheric dynamo: ICON-MIGHTI and Swarm observations of extreme neutral winds and currents [Preprint]. https://doi.org/10.1002/essoar.10510816.2

Heki, K. (2006). Explosion energy of the 2004 eruption of the Asama Volcano, central Japan, inferred from ionospheric disturbances. *Geophysical Research Letters, 33*(14), https://doi.org/10.1029/2006gl026249

Huang, C. Y., Burke, W. J., Machuzak, J. S., Gentile, L. C., & Sultan, P. J. (2001). DMSP observations of equatorial plasma bubbles in the topside ionosphere near solar maximum. *Journal of Geophysical Research: Space Physics, 106*(A5), 8131–8142. https://doi.org/10.1029/2000ja000319

Igarashi, K., Kainuma, S., Nishimuta, I., Okamoto, S., Kuroiwa, H., Tanaka, T. et al. (1994). Ionospheric and atmospheric disturbances around Japan caused by the eruption of Mount Pinatubo on 15 June 1991. *Journal of Atmospheric and Terrestrial Physics, 56*(9), 1227–1234. https://doi.org/10.1016/0021-9169(94)90060-4

Johnson, J. B. (2007). On the relation between infrasound, seismicity, and small pyroclastic explosions at Karymsky Volcano. *Journal of Geophysical Research, 112*(B8), https://doi.org/10.1029/2006jb004654

Kil, H., & Heelis, R. A. (1998). Global distribution of density irregularities in the equatorial ionosphere. *Journal of Geophysical Research: Space Physics, 103*(A1), 407–417. https://doi.org/10.1029/97ja02698

Kil, H., Paxton, L. J., & Oh, S.-J. (2009). Global bubble distribution seen from ROCSAT-1 and its association with the evening prereversal enhancement. *Journal of Geophysical Research: Space Physics, 114*(A6). https://doi.org/10.1029/2008ja013672

Kil, H., Paxton, L. J., Lee, W. K., & Jee, G. (2019). Daytime Evolution of Equatorial Plasma Bubbles Observed by the First Republic of China Satellite. *Geophysical Research Letters, 46*(10), 5021–5027. https://doi.org/10.1029/2019gl082903

Kil, H., Lee, W. K., & Paxton, L. J. (2020). Origin and Distribution of Daytime Electron Density Irregularities in the Low-Latitude F Region. *Journal of Geophysical Research: Space Physics*, *125*(9), e2020JA028343. https://doi.org/10.1029/2020JA028343

Liu, C. H., Klostermeyer, J., Yeh, K. C., Jones, T. B., Robinson, T., Holt, O. et al. (1982). Global dynamic responses of the atmosphere to the eruption of Mount St. Helens on May 18, 1980. *Journal of Geophysical Research, 87*(A8), 6281. https://doi.org/10.1029/ja087ia08p06281

Maruyama, T., & Matuura, N. (1984). Longitudinal variability of annual

changes in activity of equatorial spreadFand plasma bubbles. *Journal of Geophysical Research, 89*(A12), 10903. https://doi.org/10.1029/ja089ia12p10903

Matoza, R. S., Vergoz, J., Le Pichon, A., Ceranna, L., Green, D. N., Evers, L. G. et al. (2011). Long-range acoustic observations of the Eyjafjallajökull eruption, Iceland, April-May 2010. *Geophysical Research Letters, 38*(6). https://doi.org/10.1029/2011gl047019

McClure, J. P., Singh, S., Bamgboye, D. K., Johnson, F. S., & Kil, H. (1998). Occurrence of equatorial F region irregularities: Evidence for tropospheric seeding. *Journal of Geophysical Research: Space Physics, 103*(A12), 29119–29135. https://doi.org/10.1029/98ja02749

Nakashima, Y., Heki, K., Takeo, A., Cahyadi, M. N., Aditiya, A., & Yoshizawa, K. (2016). Atmospheric resonant oscillations by the 2014 eruption of the Kelud volcano, Indonesia, observed with the ionospheric total electron contents and seismic signals. *Earth and Planetary Science Letters*, 434112–116. https://doi.org/10.1016/j.epsl.2015.11.029

Savitzky, A., & Golay, M. J. E. (1964). Smoothing and Differentiation of Data by Simplified Least Squares Procedures. *Analytical Chemistry, 36*(8), 1627–1639. https://doi.org/10.1021/ac60214a047

Shults, K., Astafyeva, E., & Adourian, S. (2016). Ionospheric detection and localization of volcano eruptions on the example of the April 2015 Calbuco events. *Journal of Geophysical Research: Space Physics, 121*(10), https://doi.org/10.1002/2016ja023382

Stolle, C., Lühr, H., Rother, M., & Balasis, G. (2006). Magnetic signatures of equatorial spread F as observed by the CHAMP satellite. *Journal of Geophysical Research, 111*(A2), https://doi.org/10.1029/2005ja011184

Su, S.-Y., Liu, C. H., Ho, H. H., & Chao, C. K. (2006). Distribution characteristics of topside ionospheric density irregularities: Equatorial versus midlatitude regions. *Journal of Geophysical Research, 111*(A6), https://doi.org/10.1029/2005ja011330

Themens, D. R., Watson, C., Žagar, N., Vasylkevych, S., Elvidge, S., McCaffrey, A. et al. (2022). Global propagation of ionospheric disturbances associated with the 2022 Tonga Volcanic Eruption. *Geophysical Research Letters*, https://doi.org/10.1029/2022gl098158

Tsunoda, R. T. (1985). Control of the seasonal and longitudinal occurrence of equatorial scintillations by the longitudinal gradient in integratedEregion Pedersen conductivity. *Journal of Geophysical Research: Space Physics, 90*(A1), 447–456. https://doi.org/10.1029/ja090ia01p00447

Wright, C., Hindley, N., Alexander, M. J., Barlow, M., Hoffmann, L., Mitchell, C. et al. (2022). Tonga eruption triggered waves propagating globally from surface to edge of space [Preprint]. https://doi.org/10.1002/essoar.10510674.1

Zhang, S., Erickson, P. J., Goncharenko, L. P., Coster, A. J., Rideout, W., & Vierinen, J. (2017). Ionospheric Bow Waves and Perturbations Induced by the 21 August 2017 Solar Eclipse. *Geophysical Research Letters, 44*(24), https://doi.org/10.1002/2017gl076054

Zhang, S., Coster, A. J., Erickson, P. J., Goncharenko, L. P., Rideout, W., & Vierinen, J. (2019). Traveling Ionospheric Disturbances and Ionospheric Perturbations Associated With Solar Flares in September 2017. *Journal of Geophysical Research: Space Physics, 124*(7), 5894–5917. https://doi.org/10.1029/2019ja026585

Zhang, S.-R., Vierinen, J., Aa, E., Goncharenko, L., Erickson, P., Rideout, W. et al. (2022). 2022 Tonga volcanic eruption induced global propagation of ionospheric disturbances via Lamb waves [Preprint]. https://doi.org/10.1002/essoar.10510445.2

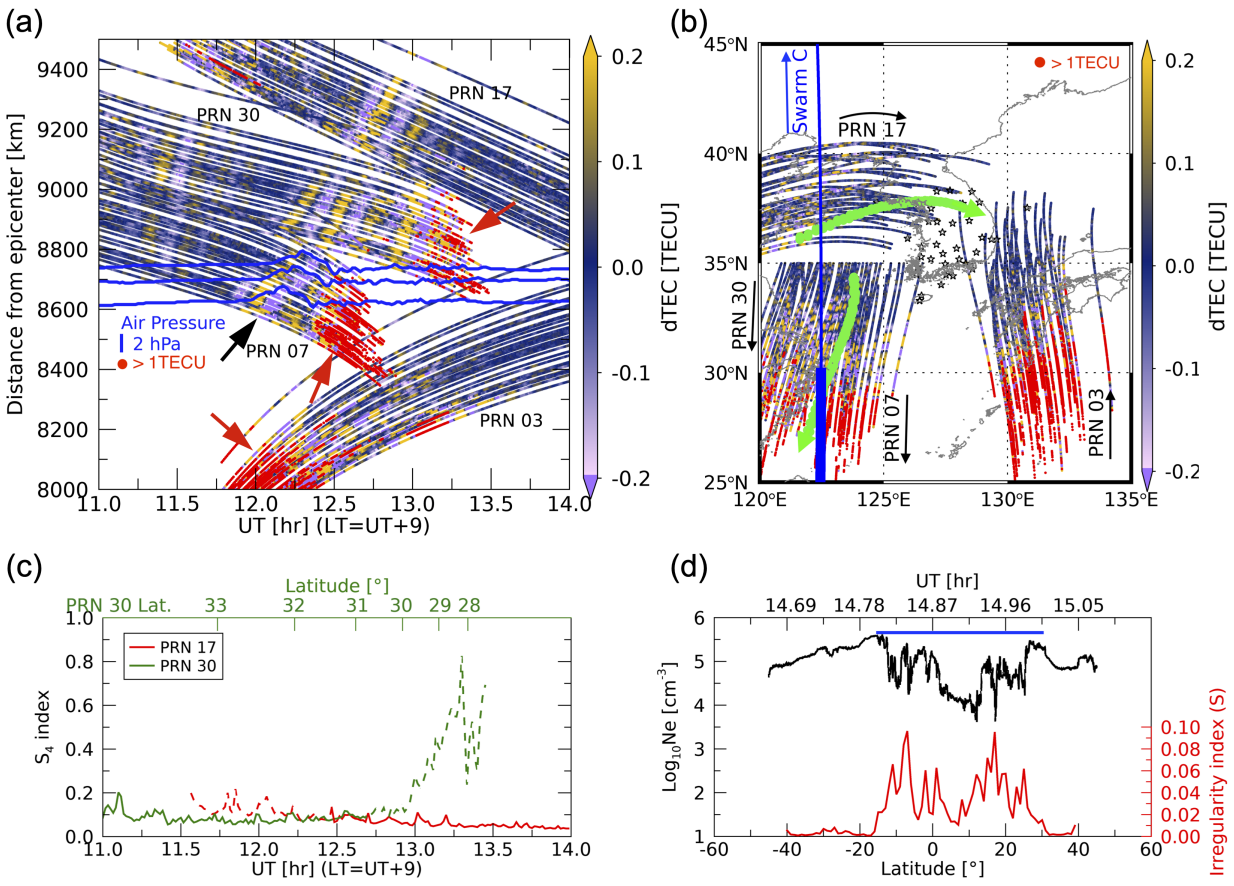

Figure 1. The ionospheric responses to the atmospheric waves induced by the

volcanic eruption. (a) The surface air pressure measurements (blue) and dTEC values (color scale) along the trajectories of PRN 3, 7, 17, and 30 as a function of UT and distance from the epicenter. The dTEC perturbations greater than 1 TECU are indicated with red dots. The black arrow indicates wave-like TEC modulations in the PRN 7, 17, and 30 trajectories detected in the west of Korea. The red arrows indicate more substantial TEC perturbations detected in the south of Korea. (b) Trajectories of the four satellites shown in Figure 1a. Black stars indicate the locations of GNSS stations. Green dots are the trajectories of GNSS satellites for the scintillation data in Figure 1c. The vertical blue line indicates the Swarm-C satellite pass with the location (thick line) of strong irregularities. (c) S_4 indices along the green dot trajectories show in Figure 1b. The data for elevations 15°–30° are distinguished by dashed lines. (d) Swarm-C measurements of the electron density (black) with the irregularity index S (red) along the blue line shown in Figure 1b.

GNSS: Global Navigation Satellite System; TEC: Total electron content; PRN: Pseudo random number

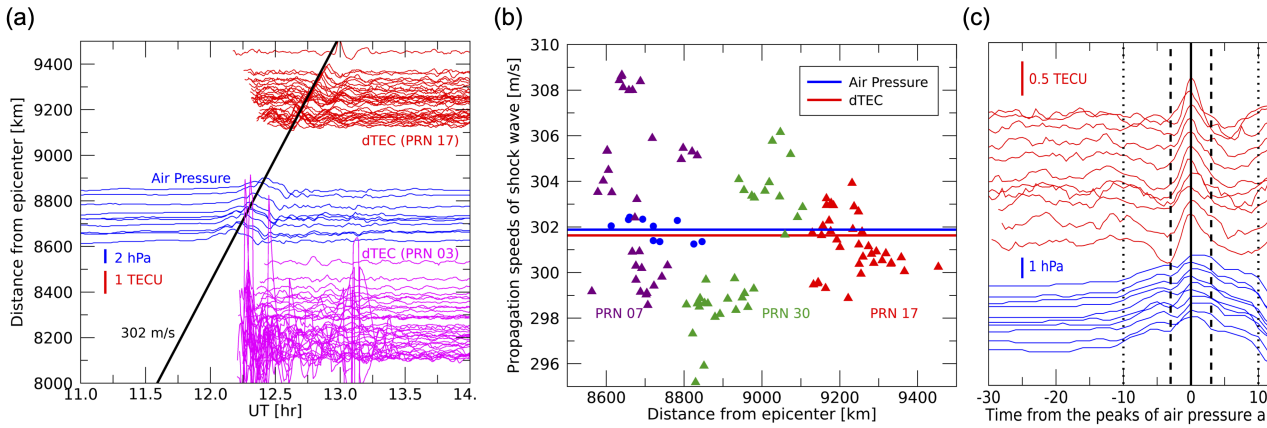

Figure 2. Derivation of the propagation speed of the TEC and surface air pressure perturbations. (a) Line plots of the surface air pressure (blue) and dTEC (PRN 3: magenta, PRN 17: red) as a function of UT and the distance from the epicenter. The black line approximately connects the peak locations of the surface air pressure and PRN 17 dTEC. This line also indicates the propagation speed (302 m/s) of the perturbations. (b) Propagation speeds of the surface air pressure perturbations (blue dots) and TEC perturbations (purple: PRN 07, green: PRN 30, red: PRN 17). The horizontal lines indicate the mean velocities from each data set. (c) Surface air pressure (blue) and PRN 17 dTEC data (red) as a function of the epoch defined as the time of the peak surface air pressure and dTEC. The black line indicates the peak locations of the perturbations. Black dashed and dotted lines indicate 3 minutes and 10 minutes from the epoch, respectively.

TEC: Total electron content; PRN: Pseudo random number

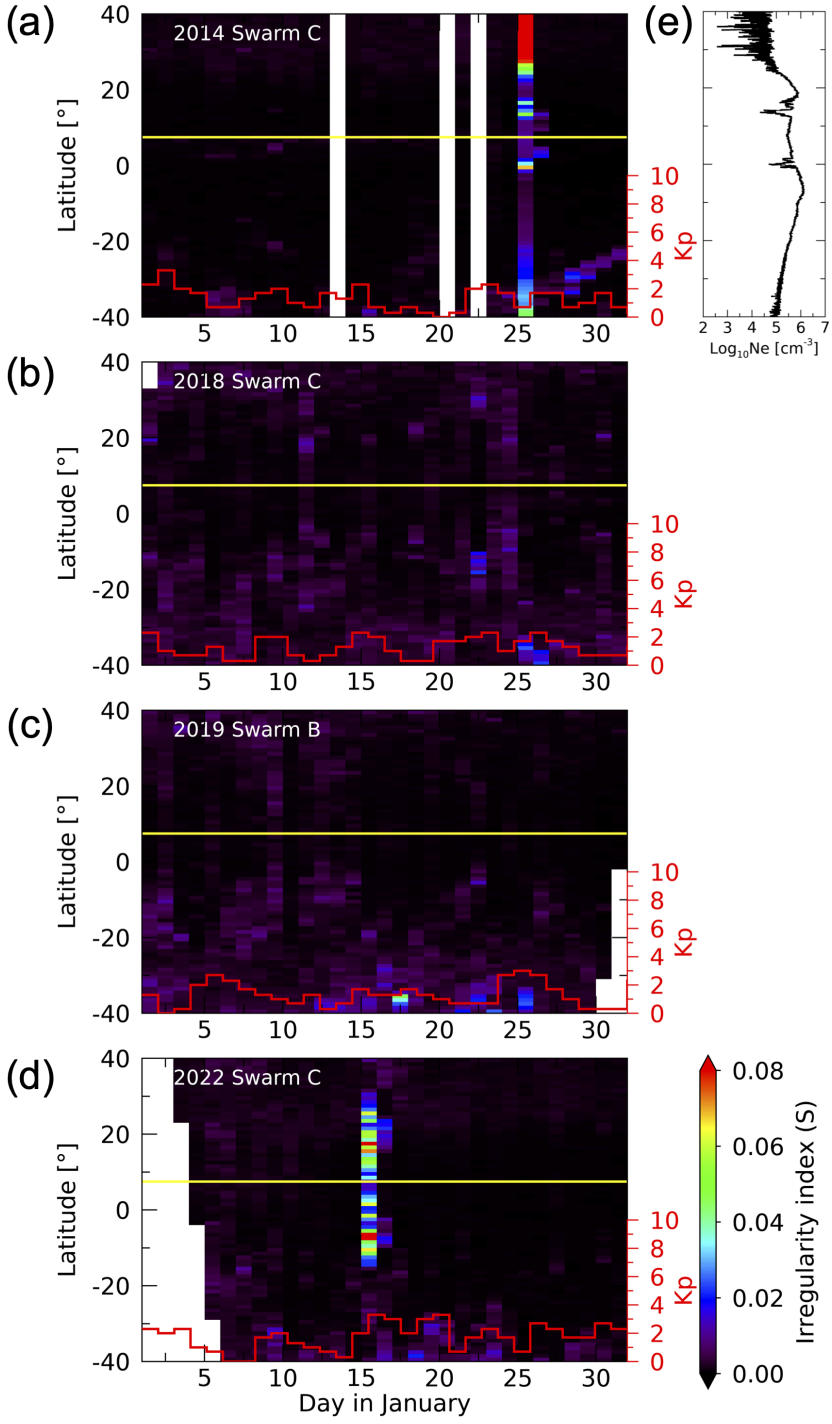
(a)
2014 Swarm C
(b)
2018 Swarm C
(c)
2019 Swarm B
(d)
2022 Swarm C
(e)
Latitude [°]
Kp
Day in January
Log10Ne [cm-3]
Irregularity index (S)

Figure 3. Occurrence climatology of irregularities in January seen by (a) Swarm-C in 2014, (b) Swarm-C in 2018, (c) Swarm-B in 2019, and (d) Swarm-C in 2022. On each day, the irregularity parameter S is calculated in each 1° bin using the data at 20–00 LT and 100°–140°E longitude. Yellow lines are the magnetic equator, and red lines present the daily mean Kp index. (e) Swarm-C electron density data on 25 January 2014.

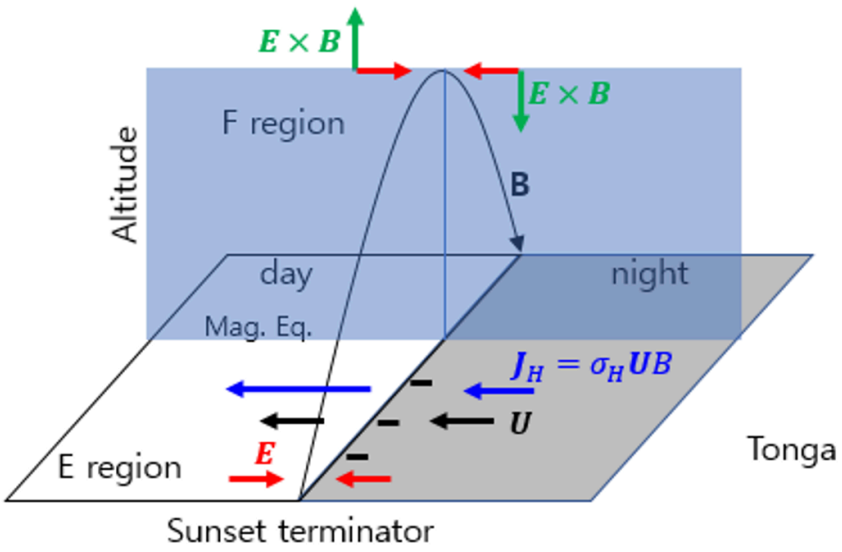

Figure 4. Schematic illustration of the dynamo process at the sunset terminator driven by neutral wind (U) from the volcanic eruption. Westward winds drive westward Hall current (J_{H}) in the E region, but the day-night difference of the Hall conductivity ($_{\mathrm{H}}$) induces the polarization electric fields (E). Mapping of these electric fields to the F region drives the upward E×B plasma drift in sunlight.